

## Article

# New Rock Magnetism and Magnetic Fabrics Studies on the Late Triassic Volcanic Rocks from Qaidam Block, Northern Tibetan Plateau

Ruiyang Chai <sup>1</sup>, Yanan Zhou <sup>1,\*</sup> , Teng Wang <sup>1</sup>, Xin Cheng <sup>1</sup>, Bitian Wei <sup>1</sup>, Nan Jiang <sup>1,2</sup>, Dongmeng Zhang <sup>1</sup>, Longyun Xing <sup>1</sup>, Pengfei Wang <sup>1</sup>, Dongwei Liu <sup>1</sup>, Ziwei Bian <sup>1</sup>  and Hanning Wu <sup>1</sup>

<sup>1</sup> State Key Laboratory of Continental Dynamics, Department of Geology, Northwest University, Xi'an 710069, China; chairuiyang2022@163.com (R.C.); wangteng921203@163.com (T.W.); chengxin@nwu.edu.cn (X.C.); wei790712301@163.com (B.W.); jnnwu2017@163.com (N.J.); dm69974@163.com (D.Z.); xly2424270471@163.com (L.X.); aldnoahwang@163.com (P.W.); 18730060753@163.com (D.L.); 202110382@stumail.nwu.edu.cn (Z.B.); wuhn2506@nwu.edu.cn (H.W.)

<sup>2</sup> School of Petroleum Engineering and Environment Engineering, Yan'an University, Yan'an 716000, China

\* Correspondence: zhouyanan@nwu.edu.cn

**Abstract:** The Qaidam Block, located at the northern Qinghai–Tibet Plateau, is a pivotal area in unraveling the closure time of the Kunlun Ocean basin which might have recorded the transformation process between the Proto-Tethys and Paleo-Tethys Ocean basins. However, the late Triassic position of the Qaidam Block remains enigmatic, largely due to the scarcity of paleomagnetic data essential for quantitatively determining its paleolatitude. The widespread presence of the Elashan formation, particularly along the southern periphery of the Qaidam block, presents good material for conducting paleomagnetic work. Nevertheless, the primary magnetic carriers preserved within the Elashan formation might be influenced by multiple tectonic thermal events, particularly those associated with collisions between southern blocks and the Qaidam Block. Here we present rock magnetism and magnetic fabrics studies to identify the content and composition of magnetic minerals within the Elashan formation. The rock magnetic and petrologic results show that the magnetic carriers in the samples from the Elashan formation are dominated by magnetite with a small amount of goethite, pyrrhotite, and hematite. The results of Anisotropy in Magnetic Susceptibility indicate that the south of the Longwalangku section might not be obviously influenced by the tectonic events. Our results also provided guidance for future paleomagnetic research, emphasizing the importance of conducting further sampling away from adjacent faults, particularly in the southern Longwalangku area.

**Keywords:** late Triassic; Elashan formation; rock magnetism; Anisotropy in Magnetic Susceptibility; Qaidam block; paleomagnetism



**Citation:** Chai, R.; Zhou, Y.; Wang, T.; Cheng, X.; Wei, B.; Jiang, N.; Zhang, D.; Xing, L.; Wang, P.; Liu, D.; et al. New Rock Magnetism and Magnetic Fabrics Studies on the Late Triassic Volcanic Rocks from Qaidam Block, Northern Tibetan Plateau. *Minerals* **2024**, *14*, 515. <https://doi.org/10.3390/min14050515>

Academic Editor: Matteo Maron

Received: 27 March 2024

Revised: 9 May 2024

Accepted: 12 May 2024

Published: 15 May 2024



**Copyright:** © 2024 by the authors. Licensee MDPI, Basel, Switzerland. This article is an open access article distributed under the terms and conditions of the Creative Commons Attribution (CC BY) license (<https://creativecommons.org/licenses/by/4.0/>).

## 1. Introduction

The Qaidam Block (QB) is in a pivotal position that connects the East Kunlun Orogenic Belt (EKOB) to the south and the Qilian Orogenic Belt to the north [1–4]. EKOB, as a relic of the Kunlun Ocean basin, was formed by the accretion of a series of continental fragments, ophiolitic melange, and interoceanic islands from the Paleozoic to early Mesozoic, recording a complicated transformation process from the Proto- to Paleo-Tethyan Oceans [3,5,6]. The collision between the North Qiangtang Block (NQB) and the QB caused the destruction of the Kunlun Ocean basin. The closure time of the Kunlun Ocean should be the middle-to-late Permian, which was indicated by the angular unconformity between the late Permian of the upper Gequ Formation and middle Permian of the lower Maerzheng Formation along the Maerzheng–Buqingshan orogenic zone [7]. However, the late Triassic mafic dikes and felsic volcanic rocks (228~218 Ma) in the EKOB were characterized with a post-collisional setting, indicating that the Kunlun Ocean was closed before the Early–Middle Triassic

or the Late Triassic [5,6,8–11]. These disputes hinder not only the understanding of the closure time of the Kunlun Ocean basin but also the tectonic evolution from Proto-Tethys to Paleo-Tethys domains.

Paleomagnetism is one of the most effective methods for paleogeographic reconstruction. The final collision between the northern and southern blocks of EKOB caused the closure of the Kunlun Ocean basin. However, the collision time of the North Qiangtang Block (NQB) and the QB remains enigmatic, largely due to the scarcity of paleomagnetic data essential for quantitatively determining its paleolatitude. Reliable paleomagnetic data from the late Permian to late Triassic published recently showed the NQB was located at  $\sim 1.0^\circ$  N during 252–247 Ma [12],  $\sim 5.4^\circ$  S during  $\sim 250$  Ma [13],  $\sim 5.6^\circ$  N during 242–240 Ma [14], and  $\sim 37^\circ$  N during 237–201 Ma (reference site:  $36.8^\circ$  N,  $98.0^\circ$  E) [13,15]. Whereas, reliable paleomagnetic results from the northern block (QB) of the Kunlun Ocean are relatively scarce [8,15]. Recently, the paleomagnetic results from three different locations along the southern margin of QB have revealed a similar paleolatitude ( $14$ – $20^\circ$  N). The author suggests the closure time of the Kunlun Ocean is the Early–Middle Triassic [8], which is based on the 37 paleomagnetic directions. This result hardly fulfills the international paleomagnetic data evaluation criterion [16]. More Triassic paleomagnetic data are needed.

The Elashan formation is well exposed along the south of the QB, composed of mafic-intermediate volcanic rocks, and the age is constrained by Zircon U–Pb geochronology (228–218 Ma; see next section), which is a good material to conduct paleomagnetic work. However, multiple tectonic thermal events related to collisions between the blocks, including the NQB, South Qiangtang block, and Lhasa Block, amalgamated with the QB [3,6,13,17–20], which might have affected the primary magnetic minerals in the Elashan formation. To identify the type of magnetic minerals that persevered in the Elashan formation, the results of rock magnetism, petrology, and demagnetization were analyzed. Moreover, the magnetic fabrics were used to analyze the influence of tectonic events.

## 2. Geological Setting and Sampling

The QB is located in the northern Tibetan Plateau (Figure 1a), separated from the Tarim Block and North China Block by the Altyn Tagh fault to the west and Qilian Orogen to the north. Most of the area of the QB is covered by thick Cenozoic successions, while the Elashan formation is mainly exposed along the south of the Qaidam block near the EKOB.

The Elashan formation, formed in the late Triassic [5,9], consists of abundant basalt, trachyandesite, trachyte, andesite, rhyolite, and pyroclastic rocks. In the Dulan area, the exposure comprises mainly andesites and interbedded dacite tuff and tuff breccias (Figure 1c, BGMRQP 1991). The age of the Dulan samples was constrained to be the middle-to-beginning stage of the late Triassic (ranging from 243 to 235 Ma) by Zircon U–Pb geochronology [21]. Further results revealed the later age for the Elashan formation south of the QB. The zircon U–Pb ages of volcanic rocks of the Elashan formation in the Dulan–Xiangride Basin are 227.9–217.9 Ma [5]. A similar result (228–218 Ma) was reported by dating the zircon from the mafic dikes (diabase) and felsic volcanic rocks (rhyolitic tuff and rhyolite porphyry) [9]. Moreover, late Triassic fossils (e.g., *N. nathorsti* Ertman, *N. carcinoides* Harris, and *N. carrei* (Zeiller) Halle) in argillaceous slate fine sandstone were identified from the upper part of the Elashan formation [5]. Thus, the Elashan-formation volcanic rocks were likely formed in the late Triassic.

In this study, we collected a total of 211 oriented ignimbrites samples (15 sites) from the Elashan Formation in the Dulan area ( $37.25^\circ$  N,  $96.59^\circ$  E; Figure 1c). Nine sites were collected as hand specimens along the section south of the Longwalangku area. The other six sites were collected by a portable gasoline-powered drill and oriented by a magnetic and solar compass (Figure 1c). The discrepancy in declination between these two orienting techniques is insignificant, implying that any local magnetic disturbance can be considered negligible. In this study, a total of 211 ignimbrite samples were measured for the anisotropy of magnetic susceptibility (AMS) and are representative samples for rock magnetism experiments.

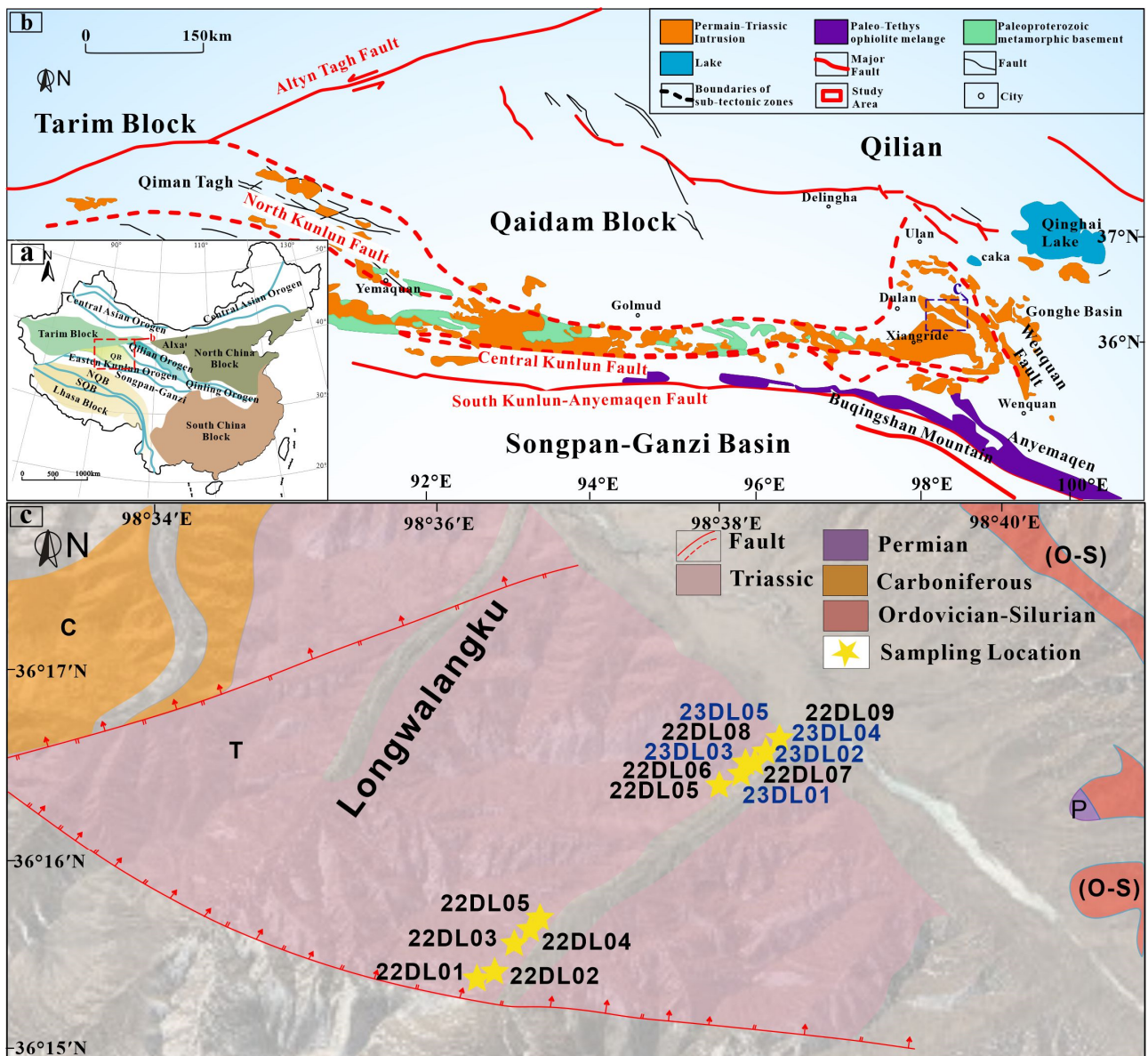


**Figure 1.** (a) Tectonic outline of the China mainland (modified from [22,23]). And showing the location of Figure 1b in the red square. (b) Regional geological map showing the location of the Qaidam Block and surrounding blocks, major faults, and Central China Orogenic Belt (modified from [24]). (c) A simplified partial geologic map of the Dulan area (modified from [25]) which shows the locations of the paleomagnetic samples.

### 3. Laboratory Techniques

#### 3.1. Rock Magnetism

We conducted the rock magnetic experiments in the Paleomagnetic Laboratory of Northwest University (Xi'an, China). The representative volcanic rock samples were selected for saturation isothermal remanent magnetization (IRM) and reverse field demagnetization experiments, the thermal demagnetization of 3-axis IRM, and *k*-T experiments. The instruments for IRM and reverse field demagnetization are the ASC IM-10-30 pulse magnetizer and JR-6A magnetometer. A DC field was applied on the sample stepwise increasing until 2.7 T. According to the saturation state of IRM under different external fields, the main types of magnetic minerals in the sample can be determined. The Cumulative log–Gaussian (CLG) curve model was also simulated in this IRM [26]. According to the characteristic that magnetic minerals with different coercivity have different unblocking

temperatures, we carried out the 3-axis IRM (the experimental equipment used in this experiment are the ASC IM-10-30 pulse magnetometer, TD-48 thermal demagnetization furnace, and JR-6A magnetometer) to obtain the thermal demagnetization curve of the 3-axis IRM. *k*-T experiments were conducted in the air using an MFK1 susceptibility meter and its CS-4 temperature control system.

### 3.2. Magnetic Fabric

Magnetic fabric is represented by the maximum (K1), the middle (K2), and the minimum (K3) axes of the magnetic susceptibility ellipsoid. The main susceptibility axes are determined by many important magnitude parameters, including the average magnetic susceptibility (Km) [27], anisotropy degree (Pj) [28], shape factor (T) [29], magnetic foliation (F) [30], and magnetic lineation (L) [31]. The magnetic fabric was measured at the State Key Laboratory of Continental Dynamics, Northwest University (Xi'an, China). All samples underwent an anisotropy of magnetic susceptibility (AMS) measurement using an MFK1-FB Kappabridge susceptibility meter (Test field strength  $300 \text{ A}\cdot\text{m}^{-1}$ , detection limit  $2 \times 10^{-8} \text{ SI}$ , test accuracy 1%) from Advanced Geoscience Instruments Company (AGICO), Czech Republic, at room temperature (operating frequency 975 Hz). The results were analyzed in Anisoft version 6 software.

### 3.3. SEM and EDS

To further illustrate the textural relationships and diagenetic conditions of the magnetic minerals, the SEM (scanning electron microscope) with EDS (Energy Dispersive Spec) was utilized to directly observe and analyze the polished thin sections of the representative samples at the State Key Laboratory of Continental Dynamics, Northwest University.

### 3.4. Demagnetization

Thermal demagnetization experiments were carried out in a magnetically shielded laboratory at the Paleomagnetic Laboratory of Northwest University (Xi'an, China). The thermal demagnetization experiment was performed using the TD-48 thermal demagnetization furnace. And the magnetic remanence was measured by the 2G-755 superconducting magnetometer. The demagnetized directions were displayed by vector analysis in the orthogonal vector diagrams [32].

## 4. Results

### 4.1. IRM

The IRM acquisition curves of the Elashan formation are shown in Figures 2 and 3. The remanent magnetization of five samples grows steadily before 0.15 T and reaches saturation before 2.5 T. According to the results, our samples could be divided into two types: Type A (22DL07, 22DL08, and 22DL09; Figure 2) reached 90% saturation faster and can be modeled by two coercivity components; Type B (22DL05 and 22DL06; Figure 3) reached 90% saturation relatively slowly and has three components. According to the coercivity spectrum, the results of the lower coercivity component (component 1; <80 mT), the intermediate coercivity component (component 2; <300~500 mT), and the high coercivity component (Component 3; >1000 mT) were obtained to analyze the information of carrying magnetic minerals. Component 1 contributes up to ~85% of the whole SIRM in Type B and ~95% in Type A. Component 2 is only obtained by analyzing Type B, which contributes up to ~8%. Each sample contains a small amount of the high coercivity magnetic carriers. Therefore, we infer that the low coercivity components predominate in the samples from the south of the Longwalangku area.

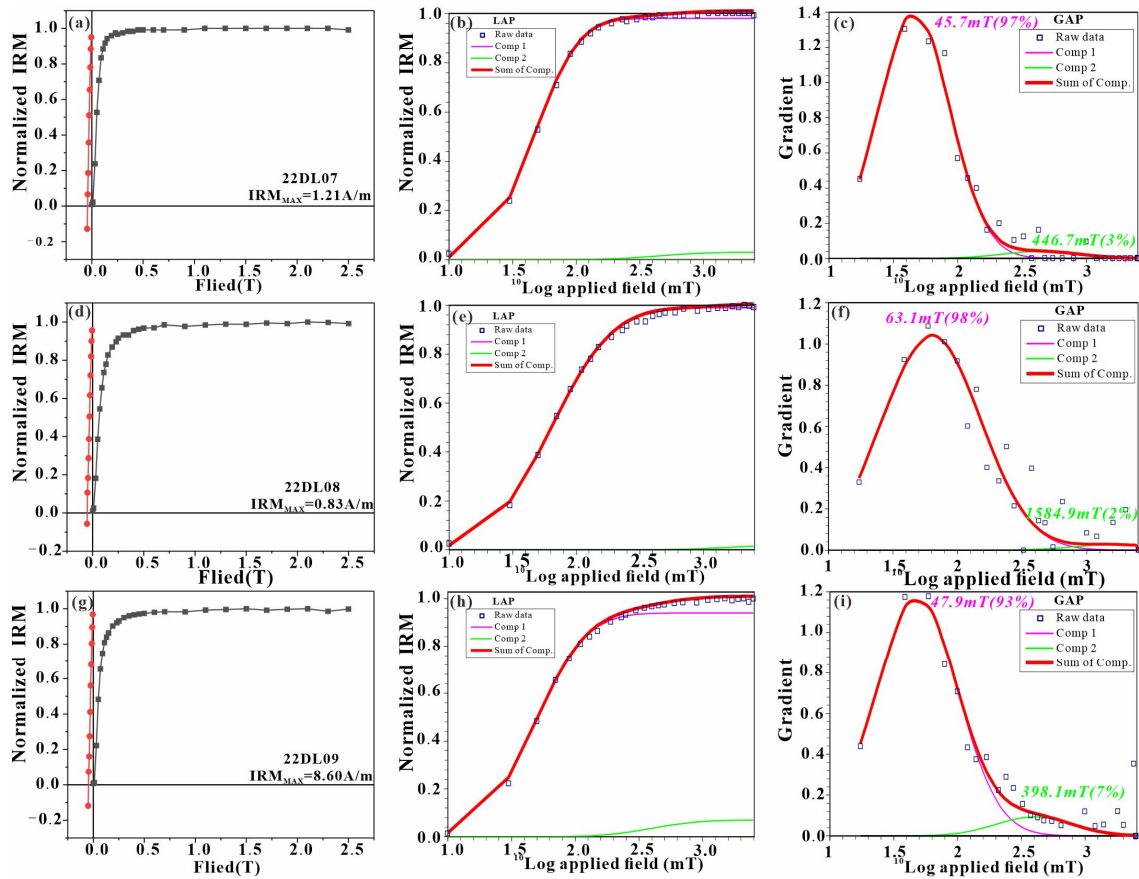


**Figure 2.** The IRM for the representative samples on Type A from the Elashan Formation. Acquisition curves of IRM and back-field demagnetization curves of IRM (a,d,g); LAP curves (b,e,h) and GAP curves (c,f,i) from Cumulative Log Gaussian analysis.

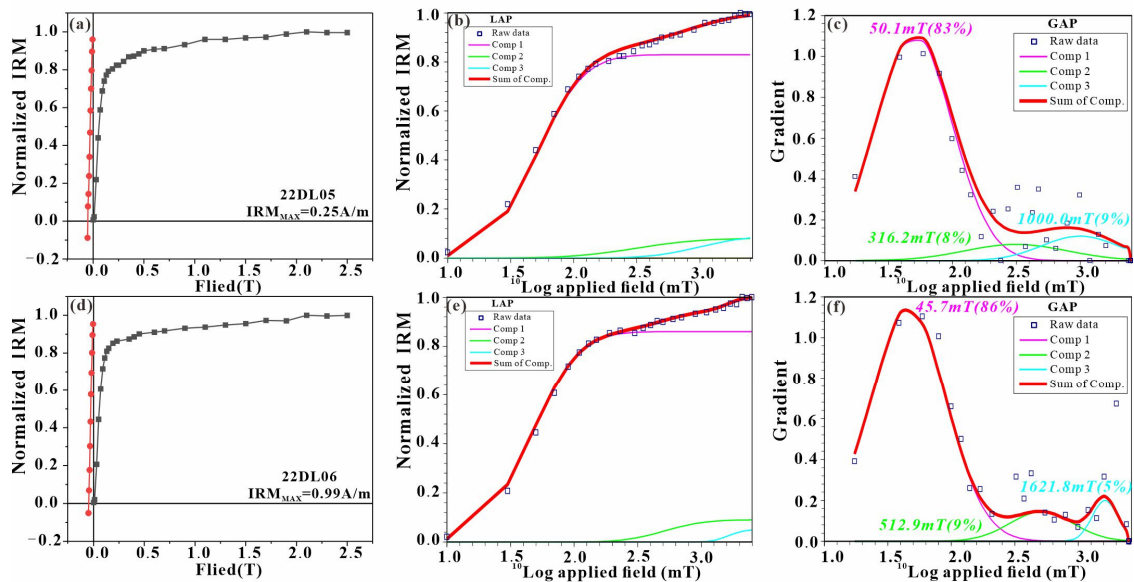


**Figure 3.** The IRM for the representative samples on Type B from the Elashan Formation. Acquisition curves of IRM and back-field demagnetization curves of IRM (a,d); LAP curves (b,e) and GAP curves (c,f) from Cumulative Log Gaussian analysis.

#### 4.2. Thermal Demagnetization of Three-Axis IRM

The three-axis IRM curves of the Elashan formation show that the soft components have a predominant role in the magnetic minerals and are unblocked at  $\sim 560\text{--}580\text{ }^{\circ}\text{C}$  (Figure 4). The hard and medium components have a similar contribution in the 22DL05 and 22DL06. The hard component curve of 22DL05 has decreased abruptly below  $120\text{ }^{\circ}\text{C}$ , which suggests that there may be a small amount of goethite [33]. The hard component curves of 22DL05 and 22DL06 gradually decreased and reached zero at  $680\text{ }^{\circ}\text{C}$ , which suggests that there may be a small amount of hematite. The samples 22DL07 and 22DL08 might have some iron-sulfides (e.g., pyrrhotite, melnikovite) because of the slight decrease of the medium component at the range of  $300\text{--}330\text{ }^{\circ}\text{C}$ . In the hard and medium component curves of 22DL09, they completely unblocked at  $\sim 610\text{ }^{\circ}\text{C}$ , which indicated that a small amount of maghemite existed in the samples. Hence, we inferred that the magnetic minerals in the samples were composed of magnetite, goethite, maghemite, pyrrhotite, and hematite.

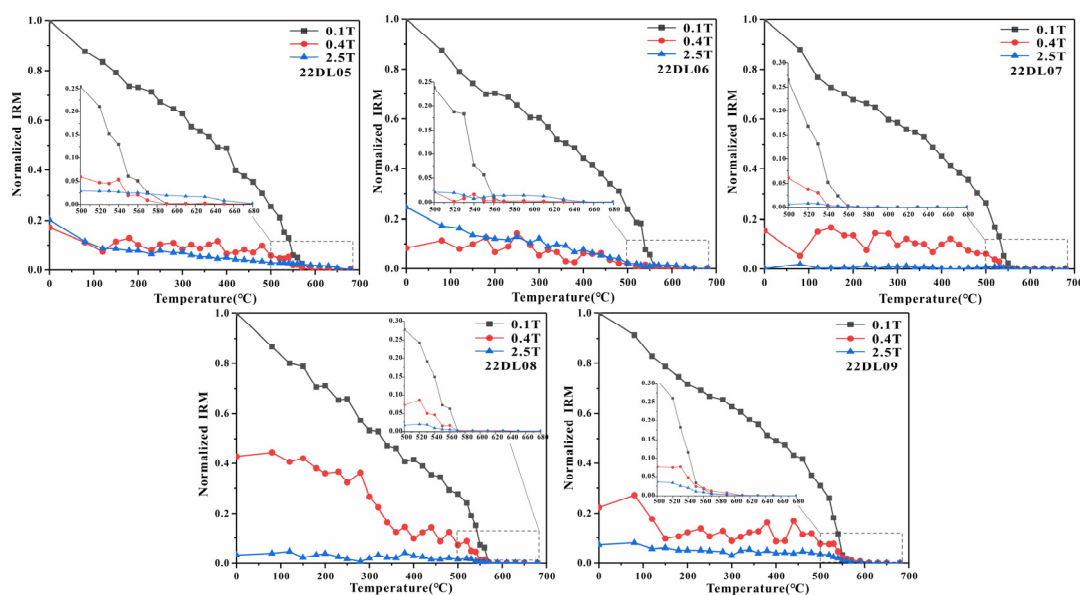


**Figure 4.** Thermal demagnetization of the IRM in three orthogonal axes for the representative samples from Elashan formation.

#### 4.3. $k$ - $T$

The  $k$ - $T$  curves we obtained (Figure 5) from the representative samples mainly included three types: (1) The heating and cooling curves were basically reversible, indicating that there may be less mineral phase transformation during the experimental process. Magnetic susceptibility significantly decreased in the initial heating process, which may be caused by goethite or paramagnetic minerals unblocked. There was an increase before  $420\text{ }^{\circ}\text{C}$  and a rapid decrease after  $\sim 580\text{ }^{\circ}\text{C}$ , and the heating curves finally decreased to zero until  $680\text{ }^{\circ}\text{C}$ . (2) The cooling curves are clearly higher than the heating curves below  $\sim 530\text{ }^{\circ}\text{C}$  in the 22DL06, indicating the thermal alteration of other Fe-bearing minerals to a new magnetite phase during heating. An increased phase in the heating curves of 22DL06 occurred between  $240$  and  $300\text{ }^{\circ}\text{C}$ . This may be due to the dehydration of lepidocrocite ( $\gamma\text{-FeO(OH)}$ ), homogeneous and polymorphic with goethite) and its transformation into maghemite [34,35]. In addition, the heating curves of 22DL06 have a slight increase at  $400$  and  $500\text{ }^{\circ}\text{C}$ . The transformation from clay minerals or iron sulfides into magnetite might cause susceptibility to increase during the temperature increase [36,37]. (3) There is a distance between the cooling curve and heating curve before  $550\text{ }^{\circ}\text{C}$  in the 22DL09, indicating that new minerals with higher susceptibility were generated during the heating process.

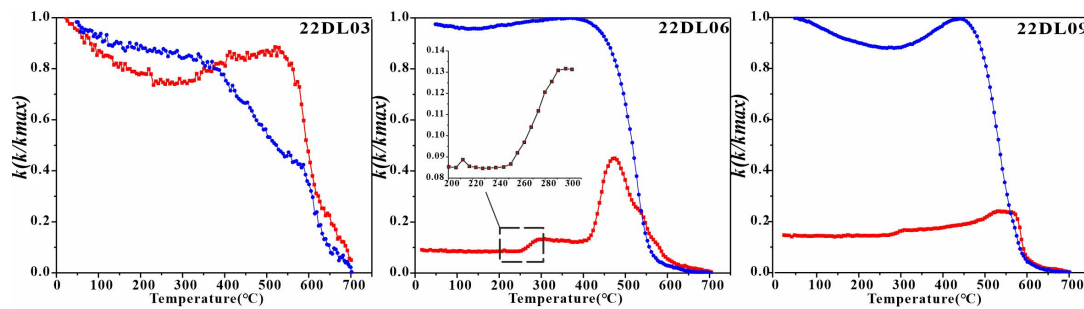


**Figure 5.**  $k$ - $T$  curves (the red/blue solid lines are heating/cooling curves) of representative samples from Elashan formation.

#### 4.4. Magnetic Fabric

The Flinn diagram is the initial expression of the magnetic susceptibility ellipsoid [38]. Most of the sampling points fall in the right area of the line ( $F = L$ ) in the Flinn diagram, which shows that the magnetic susceptibility ellipsoid is a flattened situation (Figure 6a), and the development of magnetic foliation is stronger than magnetic lineation. Similarly, the majority of sample shape factors ( $T$ ) are greater than 0, which also indicates a flattened magnetic susceptibility ellipsoid. The value of the anisotropy degree ( $P_j > 1$ ) shows that the result in this study is consistent with the characteristic of the undeformed clastic rocks [39] (Figure 6b). The anisotropy degree is positively correlated with magnetic foliation, not with magnetic lineation (Figure 6c,d), which indicates that the anisotropy degree was controlled by the magnetic foliation. The average magnetic susceptibility ( $K_m$ ) is affected by magnetic minerals, which reflects the comprehensive characteristics of the magnetic susceptibility for magnetic minerals [29]. The average magnetic susceptibility ( $K_m$ ) also can reflect the type of magnetic minerals. The  $K_m$  of Elashan formation samples is low with an average value of  $238.5 \times 10^{-6}$  SI. Therefore, the paramagnetic minerals also exist in our samples. The intrusion mode of volcanic rocks can be distinguished by the parameter  $f$  ( $f = K_1 / \sqrt{K_2 K_3}$ ) [40,41]. Almost all samples indicated the characteristic effusive rock ( $f < 1.04$ ).

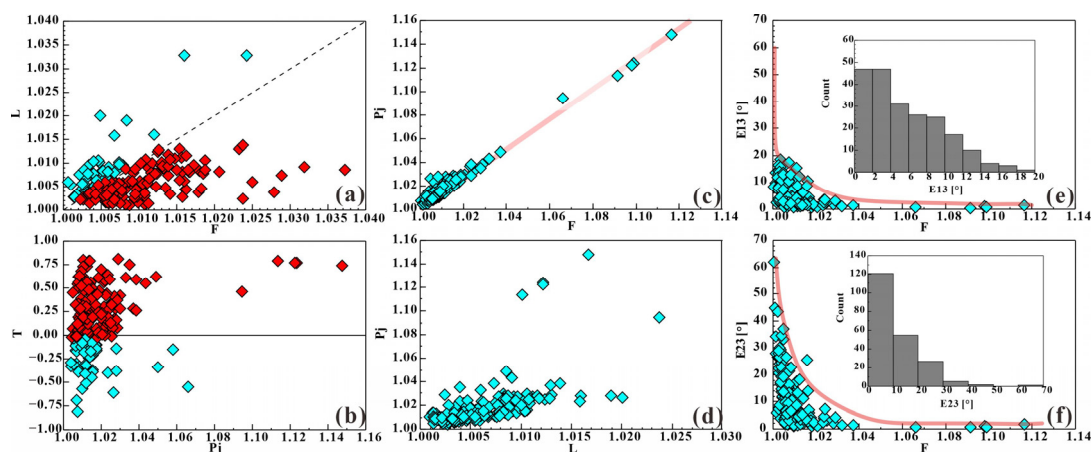


**Figure 6.** The relationship of the AMS parameters. (a): the relationship between the  $F$  and  $L$ ; (b): the relationship between the  $P_j$  and  $T$ ; (c): the relationship between the  $F$  and  $P_j$ ; (d): the relationship between the  $L$  and  $P_j$ ; (e): the relationship between the  $F$  and  $E_{13}$ ; (f): the relationship between the  $F$  and  $E_{23}$ ; (in (a,b), the red points represented Oblate and the blue points represent Prolate).

#### 4.5. SEM and EDS Analyses

According to the SEM image observation with EDS analysis, iron oxides could be found in the samples from the south of the Longwalangku section (Figure 7). The size of iron oxides is ranged from 13 to 130  $\mu\text{m}$ . Most of them are exhibiting euhedral to irregular

shapes (Figure 7). However, it was found that some iron sulfide adhered to iron oxide minerals (EDS Spot 1, Figure 7). Combined with the results of rock magnetism in the previous sections, a slight decrease in the medium component of the 3-axis IRM curves from samples 22DL07 and 22DL08 is observed in the temperature range of 300–330 °C. As a preliminary inference, we suggest that the iron oxide and iron sulfide minerals may be magnetite and pyrrhotite. The boundary of the iron oxide minerals and matrix is distinct. The phenomenon of oxidized edges is not observed among the numerous results of SEM, and cracks also do not widely exist. Therefore, the samples are less affected by thermal erosion and tectonic activity.

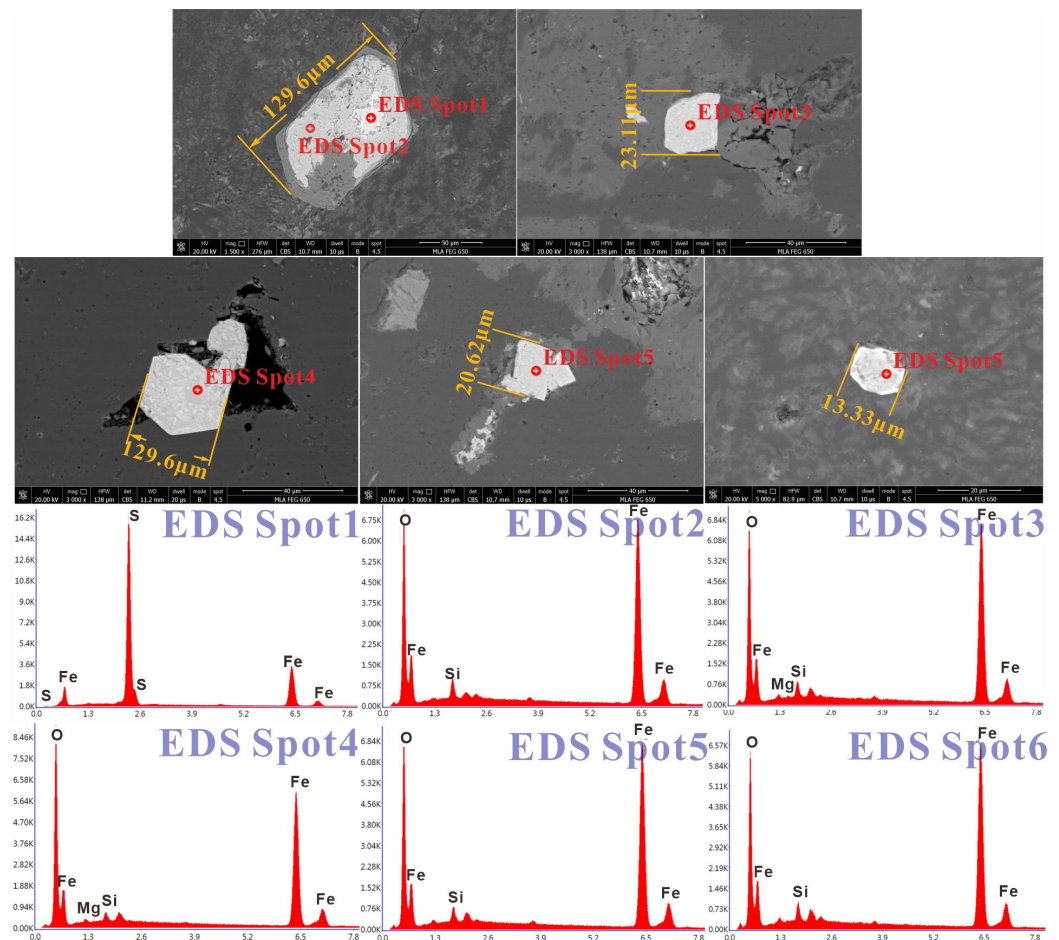


**Figure 7.** Scanning electron microscope (SEM) images and the results of the energy dispersive spectroscopy (EDS) analyses of the samples from the Dulan area.

#### 4.6. Demagnetization

The information of magnetic carriers in the samples could be displayed by the zijderveld diagrams and the intensity of the demagnetization behaviors curves. Fifty-five paleomagnetic core specimens from six sites were demagnetized to obtain the directions and normalized intensity behaviors curves. The demagnetization of the south of the Longwalangku area was characterized by two components, including a high-temperature component (HTC) and a low-temperature component (LTC) (Figure 8). The LTC was removed by approximately 400 °C and the HTC was isolated between 450 and 580 °C (Figure 8). After tilt correction, the HTCs were concentrated in a similar direction.

In normalized intensity behaviors curves, the remanent intensity showed a relatively stable trend of rise, which means that two different components existed. The stable rise of the remanent intensity is consistent with the results of the zijderveld diagrams. However, several lines decrease during the NRM to 150 °C, which might be caused by the unblocking

of goethite. The curves rapidly approached the original point after 500 °C and reached it at ~580 °C in the zijderveld diagrams. Meanwhile, the intensity decreased quickly and almost decayed to near zero at ~580 °C, which indicates the existence of magnetite. However, other magnetic minerals could not be identified from the zijderveld diagrams and the normalized intensity of the demagnetization behaviors curves.

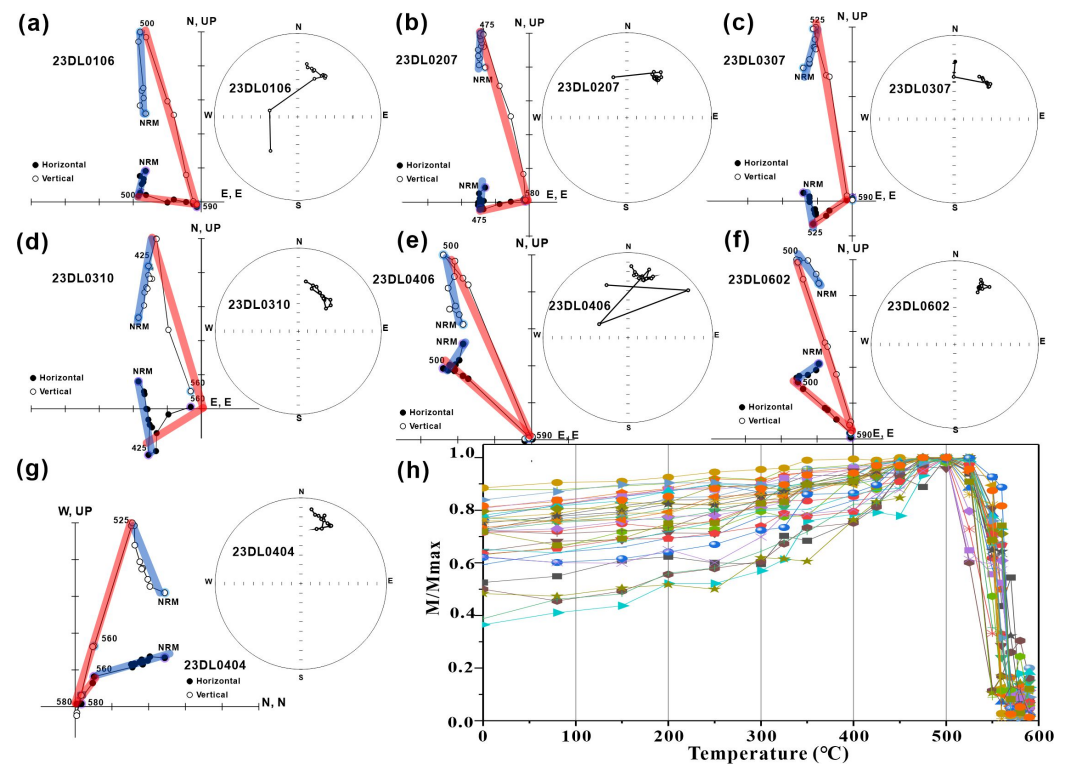


**Figure 8.** (a–g) Representative thermal demagnetization results. All results are shown in geographic coordinates. In the orthogonal vector plots, filled (open) circles depict the horizontal (vertical) component; in the stereonet insets, filled (open) circles depict projections on the lower (upper) hemisphere. The red/blue lines in orthogonal vector plots were used for fitting the high/low-temperature components. (h) The normalized magnetic moment versus temperature of samples from Elashan Formation.

## 5. Discussion

The formation of Elashan volcanic rocks might be attributed to the magmatic activity generated by the collision of southern plates from the QB, which caused the destruction of the Kunlun Ocean basin [2,3,42]. Multiple tectonic thermal events particularly associated with collisions involving the southern blocks of the Qaidam Block have been identified [3,6,13,17–20]. For instance, the granites (late Permian to Triassic) are widely exposed in the Dulan area, the southern part of the QB, according to the regional geological investigation [25], hinting that tectonic thermal events might be affected by the magnetic remanence signals carried by the magnetic minerals near the Dulan area. The magnetic fabrics in volcanic rocks primarily originate during lava eruption, which could be overprinted by tectonic events [43]. Therefore, ascertaining the magnetic mineral assemblages of samples and the influence of tectonic events by analyzing magnetic fabrics from the Elashan Formation is fundamental for obtaining a reliable interpretation of remanent magnetization.

### 5.1. The Magnetic Mineral Assemblage

The results of the IRM curves and CLG model analysis revealed that the magnetic minerals in the Elashan formation are predominated by low coercivity minerals, while the medium and high coercivity of magnetic minerals are also present in the samples. Moreover, the soft components, as a primary role, unblocked at ~560–580 °C, exhibited by the three-

axis IRM curves. Additionally, the heating curves decayed to zero at approximately 580 °C in the  $k$ -T curves. Furthermore, the demagnetization behaviors revealed that the HTC of 55 samples gradually decayed towards the origin within a temperature interval ranging from 500 to 580 °C. Hence, magnetite is a predominant magnetic mineral in samples from the south of the Longwalangku section. In the initial heating process, a notable decrease in the magnetic susceptibility of the  $k$ -T curves was observed, likely attributed to the goethite or paramagnetic minerals unblocked within that temperature range. Moreover, in the 22DL05 sample, the hard component curve experienced an abrupt decrease below 120 °C, and an obvious decline in the normalized intensity during the NRM to 150 °C was observed; all these signals hint at the potential existence of a minor quantity of goethite. Regarding pyrrhotite, the results of EDS indicate the presence of iron sulfide minerals within the samples. Additionally, a slight decrease in the medium component of the three-axis IRM curves was observed at the temperature range of 300–330 °C from the samples 22DL07 and 22DL08, suggesting the existence of pyrrhotite.

According to the analysis of the demagnetization, rock magnetic, and petrologic results, we inferred that the magnetic minerals in the volcanic rocks of the Elashan formation are as follows: (1) Magnetite, as the main magnetic carriers, carried the stable high-temperature component. (2) Other magnetic minerals with a lower content in the samples cannot be ignored (goethite, pyrrhotite, and hematite).

### 5.2. Analysis of Magnetic Fabrics

Two methods have been proposed to discern the primary fabric or secondary fabric: (1) The lower value of the anisotropy degree ( $P_j < 1.2$ ) is indicative of a primary magnetic fabric [39,44,45]. (2) An examination of microstructures to rule out the presence of fracturing, crystal plasticity, and recrystallization phenomena [46]. In this study, the site-mean values of  $P_j$  from the Elashan formation exhibited slight variation, ranging from 1.0095 to 1.0282 (Table 1). Additionally, the anisotropy degree ( $P_j$ ) displayed no discernible correlation with the average magnetic susceptibility ( $K_m$ ) (Figure 9a). Moreover, the specimens consist of rhyolite or dacite rock fragments fused with tuff by the observation of thin sections. The deformation characteristics, such as fracturing, crystal plasticity, or recrystallization resulting from post-magmatic transformation, were not observed in these samples (Figure 9b). In paleogeographic coordinates, the points of K1, K2, and K3 have an unobvious concentration phenomenon in the stereonet plots (Figure 10a). Therefore, we propose that this section was not significantly affected by multiple tectonic thermal events.

**Table 1.** Magnetic parameters of sites-mean from the Elashan formation after correction for bedding orientation.

Sites	Kmean (10 <sup>-6</sup> SI)	K1/Dec	K1/Inc	K2/Dec	K2/Inc	K3/Dec	K3/Inc	L	F	Pj	f
22DL01	185.44	136.30	29.58	190.51	27.08	181.38	41.32	1.0064	1.0122	1.0193	1.0125
22DL02	180.82	208.23	24.01	159.86	22.46	159.85	49.03	1.0068	1.0143	1.0221	1.0139
22DL03	165.91	206.85	29.46	190.43	20.23	155.42	47.65	1.0063	1.0118	1.0186	1.0122
22DL04	203.04	232.53	48.98	222.29	21.30	79.46	29.08	1.0082	1.0186	1.0282	1.0173
22DL05	179.02	206.08	24.40	99.15	20.68	216.45	52.10	1.0073	1.0110	1.0188	1.0128
22DL06	120.78	215.92	21.81	188.85	19.05	157.85	54.78	1.0063	1.0150	1.0225	1.0136
22DL07	165.36	165.89	26.60	238.42	29.02	164.23	39.68	1.0123	1.0100	1.0231	1.0173
22DL08	180.65	169.43	29.59	224.32	30.26	99.78	39.87	1.0042	1.0086	1.0134	1.0085
22DL09	164.97	196.37	42.00	204.65	23.84	109.81	34.68	1.0070	1.0083	1.0156	1.0111
23DL01	184.89	230.42	47.60	145.08	21.96	218.97	28.83	1.0044	1.0061	1.0106	1.0074
23DL02	172.34	223.28	20.32	126.93	23.65	176.57	52.83	1.0055	1.0059	1.0116	1.0085
23DL03	186.97	178.68	51.12	102.29	15.47	212.67	30.11	1.0050	1.0063	1.0115	1.0082
23DL04	181.54	179.45	41.54	231.26	29.95	192.92	28.93	1.0055	1.0064	1.0122	1.0088
22DL05	222.03	242.24	34.57	154.97	26.15	178.15	34.88	1.0046	1.0061	1.011	1.0077
22DL06	134.98	186.19	33.74	246.81	23.58	79.57	42.45	1.0035	1.0059	1.0095	1.0064

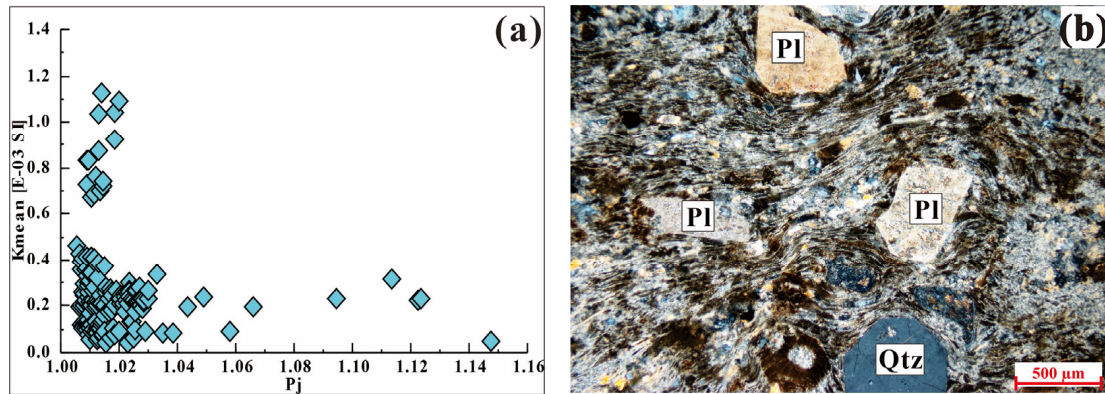


Figure 9. (a) The relationship between the  $P_j$  and  $K_{mean}$ . (b) Microscopic images of representative samples from Elashan formation. Qtz = quartz; Pl = plagioclase.

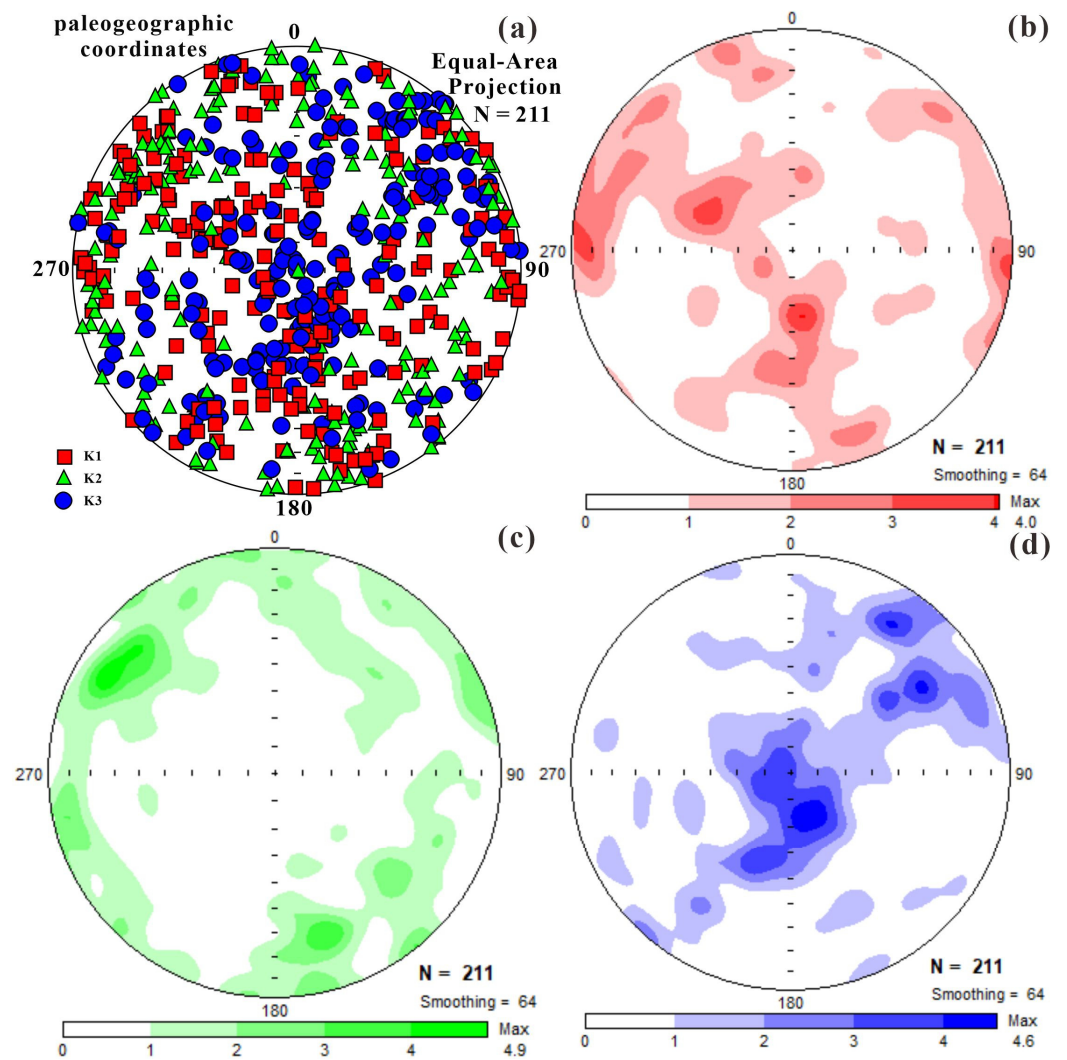


Figure 10. (a): Characteristic of magnetic fabric for the south of Longwalangku section; (b) K1 (red), (c) K2 (green), and (d) K3 (blue) for all specimens of Elashan formation in the Dulan area.

The relationship between the directions of primary magma flows and the results of the Anisotropy of Magnetic Susceptibility (AMS) analysis, specifically K1 and K3, has been documented in several studies [44,47–51]. For instance, AMS measurements conducted in the Deccan volcanic province from Western India suggest that the studied dykes predominantly exhibit a sub-vertical-to-inclined flow, with occasional sub-horizontal or lateral

flow patterns [52]. Although a clear fluxion texture and distinct plagioclase were observed in our samples (Figure 9b), the ignimbrite may not accurately record the advantageous direction by analyzing the AMS results in the southern Longwalangku area. The influence of the magma viscosity, flow velocity, and end turbulence of lavas might be affected by the direction of K1. Therefore, the reliable magma flow direction of this section could not be reconstructed well.

The mean directions of K1 and K3 are  $300.0^{\circ} \angle 11.7^{\circ}$  and  $67.1^{\circ} \angle 71.0^{\circ}$ , respectively. The inclination of K1 shows a proximity towards being horizontal-to-sub-horizontal, and the inclination of K3 approaches  $90^{\circ}$  (Table 1). According to the characteristics of the magnetic fabric from the south of the Longwalangku section in the paleogeographic coordinates, the direction of the K3 was close to the intermediate and the K1 was near the horizontal-to-sub-horizontal [41,53] (Figure 10a). As mentioned above, the AMS results of volcanic rocks from the south of the Longwalangku section indicated that the Pj of the majority of samples are low ( $<1.15$ ) and the development of magnetic foliation is stronger than magnetic lineation. Therefore, we inferred that the primitive magma flow may be in a flat state.

In the southern part of our sampling area, a normal fault crosses the Elashan Formation, suggesting that this fault formed in the post-late Triassic [25]; this fault may have formed after the Elashan Formation. By comparing the mean Pj of Section 1 (22DL01–22DL05) with Section 2 (22DL06–22DL09, 23DL01–23DL06), we can see that Section 1 ( $\sim 1.021$ ) is slightly higher than Section 2 ( $\sim 1.015$ ). To avoid the impact of this fault on the demagnetization data, we suggest that future paleomagnetic work should choose the sites in the northeast, as far away from this fault as possible.

## 6. Conclusions

In this study, we conducted a series of experiments, including rock magnetism, petrology, and AMS, on the volcanic rocks from the Upper Triassic Elashan Formation to analyze the composition of the magnetic minerals and magnetic fabric. The rock magnetism and EDS show that magnetite is the main magnetic mineral carrier, with a small amount of goethite, pyrrhotite and hematite. Oxidized edges are not obviously observed based on the SEM images. The magnetic fabric showed the characteristics of the primary fabric. According to the distribution of Anisotropy in Magnetic Susceptibility, the formation of a normal fault, near the sampling section, may have formed later than the Late Triassic, and future paleomagnetic work should choose the sites in the northeast, as far away from the adjacent fault area, in the south of the Longwalangku area, as possible. Therefore, we suggested that the section in the Dulan area is suitable for further paleomagnetic work.

**Author Contributions:** Conceptualization, R.C.; methodology, D.Z., D.L. and L.X.; software, T.W., B.W. and N.J.; formal analysis, R.C.; investigation, R.C.; resources, X.C., D.Z., P.W. and H.W.; writing—original draft preparation, R.C.; writing—review and editing, R.C.; visualization, T.W., B.W., N.J. and Z.B.; supervision, Y.Z.; project administration, Y.Z.; funding acquisition, Y.Z., X.C. and H.W. All authors have read and agreed to the published version of the manuscript.

**Funding:** This research was funded by [the National Natural Science Foundation of China] grant number [42372251, 42074075, 42274097, and 91855211]. The APC was funded by [the National Natural Science Foundation of China], grant number [42074075].

**Data Availability Statement:** The data presented in this study are available on request from the corresponding author.

**Acknowledgments:** The authors would like to thank the editors and recommenders for their insightful comments which have led to a better version of our work.

**Conflicts of Interest:** The authors declare no conflicts of interest.

## References

1. Metcalfe, I. Palaeozoic and Mesozoic tectonic evolution and paleogeography of East Asian crustal fragments: The Korean Peninsula in context. *Gondwana Res.* **2006**, *9*, 24–46. [\[CrossRef\]](#)
2. Dong, Y.P.; Sun, S.S.; Santosh, M.; Zhao, J.; Sun, J.P.; He, D.F.; Shi, X.H.; Hui, B.; Cheng, C.; Zhang, G.W. Central China orogenic belt and amalgamation of East Asian continents. *Gondwana Res.* **2021**, *100*, 131–194.
3. Zhao, G.C.; Wang, Y.J.; Huang, B.C.; Dong, Y.P.; Li, S.Z.; Zhang, G.W.; Yu, S. Geological reconstructions of the East Asian blocks: From the breakup of Rodinia to the assembly of Pangea. *Earth-Sci. Rev.* **2018**, *186*, 262–286. [\[CrossRef\]](#)
4. Xu, W.; Liu, F.L.; Dong, Y.S. Cambrian to Triassic geodynamic evolution of central Qiangtang, Tibet. *Earth-Sci. Rev.* **2020**, *201*, 103083. [\[CrossRef\]](#)
5. Fan, X.Z.; Sun, F.Y.; Xu, C.H.; Wu, D.Q.; Yu, L.; Wang, L.; Yan, C.; Bakht, S. Volcanic rocks of the Elashan Formation in the Dulan-Xiangride Basin, East Kunlun Orogenic Belt, NW China: Petrogenesis and implications for Late Triassic geodynamic evolution. *Int. Geol. Rev.* **2022**, *9*, 1270–1293. [\[CrossRef\]](#)
6. Dong, Y.P.; He, D.F.; Sun, S.S.; Liu, X.M.; Zhou, X.H.; Zhang, F.F.; Yang, Z.; Cheng, B.; Zhao, G.C.; Li, J.H. Subduction and accretionary tectonics of the East Kunlun orogen, western segment of the Central China Orogenic System. *Earth-Sci. Rev.* **2018**, *186*, 231–261. [\[CrossRef\]](#)
7. Wang, G.C.; Jia, C.X.; Zhu, Y.H.; Xiang, S.Y.; Lin, Q.X. New results and major progress in regional geological survey of the Alag Lake Sheet. *Geol. Bull. China* **2004**, *23*, 549–554. (In Chinese)
8. Huang, J.C.; Zhang, K.X.; Zhu, Y.M.; Bai, Y.S. Paleomagnetic evidence for hercynian—Indosinian tectonopaleogeographical evolution in eastern Kunlun orogenic zone. *Earth Sci.—J. China Univ. Geosci.* **1999**, *24*, 155–160. (In Chinese)
9. Hu, Y.; Niu, Y.L.; Li, J.Y.; Ye, L.; Kong, J.J.; Chen, S.; Zhang, Y.; Zhang, G.R. Petrogenesis and tectonic significance of the late Triassic mafic dikes and felsic volcanic rocks in the East Kunlun Orogenic Belt, Northern Tibet Plateau. *Lithos* **2016**, *245*, 205–222. [\[CrossRef\]](#)
10. Li, R.B.; Pei, X.Z.; Pei, L.; Li, Z.C.; Chen, G.C.; Chen, Y.X.; Liu, C.J.; Wang, M. The Early Triassic Andean-type Halagatu granitoids pluton in the East Kunlun orogen, northern Tibet Plateau: Response to the northward subduction of the Paleo-Tethys Ocean. *Gondwana Res.* **2018**, *62*, 212–226. [\[CrossRef\]](#)
11. Yang, J.S.; Wang, X.B.; Shi, R.D.; Xu, Z.Q.; Wu, C.L. The Dur'ngoi ophiolite in East Kunlun, northern Qinghai-Tibet Plateau: A fragment of paleo-Tethyan oceanic crust. *Geol. China* **2004**, *31*, 225–239. (In Chinese)
12. Cheng, X.; Wu, H.N.; Guo, Q.; Hou, B.N.; Xia, L.Y.; Wang, H.J.; Diao, Z.B.; Huo, F.F.; Ji, W.H.; Li, R.S.; et al. Paleomagnetic results of Late Paleozoic rocks from northern Qiangtang Block in Qinghai-Tibet Plateau, China. *Sci. China Earth Sci.* **2012**, *55*, 67–75. [\[CrossRef\]](#)
13. Zhou, Y.N.; Cheng, X.; Wu, Y.Y.; Kravchinsky, V.; Shao, R.Q.; Zhang, W.J.; Wei, B.T.; Zhang, R.Y.; Lu, F.R.; Wu, H.N. The northern Qiangtang Block rapid drift during the Triassic Period: Paleomagnetic evidence. *Geosci. Front.* **2019**, *10*, 2313–2327. [\[CrossRef\]](#)
14. Song, P.P.; Ding, L.; Lippert, P.C.; Li, Z.Y.; Zhang, L.Y.; Xie, J. Paleomagnetism of Middle Triassic Lavas from Northern Qiangtang (Tibet): Constraints on the Closure of the Paleo-Tethys Ocean. *J. Geophys. Res. Solid Earth* **2020**, *125*, e2019JB017804. [\[CrossRef\]](#)
15. Yu, L.; Yan, M.D.; Domeier, M.; Guan, C.; Shen, M.M.; Fu, Q.; Xu, W.L.; Xu, Z.B.; Niu, Z.C.; Yang, L.Y.; et al. New Paleomagnetic and Chronological Constraints on the Late Triassic Position of the Eastern Qiangtang Terrane: Implications for the Closure of the Paleo-Jinshajiang Ocean. *Geophys. Res. Lett.* **2022**, *49*, e2021GL096902. [\[CrossRef\]](#)
16. Meert, J.G.; Pivarunas, A.F.; Evans, D.A.D.; Pisarevsky, S.A.; Pesonen, L.J.; Li, Z.; Elming, S.; Miller, S.R.; Zhang, S.; Salminen, J.M. The magnificent seven: A proposal for modest revision of the quality index. *Tectonophysics* **2020**, *790*, 228549. [\[CrossRef\]](#)
17. Cheng, X.; Wei, B.T.; Jiang, N.; Zhou, Y.N.; Kravchinsky, V.A.; Chen, Q.L.; Xing, L.Y.; Zhang, D.M.; Li, T.; Lan, S.Q.; et al. Evolution of the North Qiangtang Block in the late Paleozoic: Paleomagnetism and its tectonic implications. *Geol. Soc. Am. Bull.* **2024**, *136*, 707–724. [\[CrossRef\]](#)
18. Huang, B.C.; Yan, Y.G.; Piper, J.D.A.; Zhang, D.H.; Yi, Z.Y.; Yu, S.; Zhou, T.H. Paleomagnetic constraints on the paleogeography of the East Asian blocks during Late Paleozoic and Early Mesozoic times. *Earth-Sci. Rev.* **2018**, *186*, 8–36. [\[CrossRef\]](#)
19. Wei, B.T.; Cheng, X.; Domeier, M.; Jiang, N.; Wu, Y.Y.; Zhang, W.J.; Wu, K.; Wang, B.F.; Xu, P.X.; Xing, L.Y.; et al. Placing Another Piece of the Tethyan Puzzle: The First Paleozoic Paleomagnetic Data from the South Qiangtang Block and Its Paleogeographic Implications. *Tectonics* **2022**, *41*, e2022TC007355. [\[CrossRef\]](#)
20. Wei, B.T.; Cheng, X.; Domeier, M.; Zhou, Y.N.; Chen, Q.; Jiang, N.; Xing, L.Y.; Zhang, D.M.; Li, T.; Liu, F.F.; et al. Paleomagnetism of Late Triassic Volcanic Rocks from the South Qiangtang Block, Tibet: Constraints on Longmuco-Shuanghu Ocean Closure in the Paleo-Tethys Realm. *Geophys. Res. Lett.* **2023**, *50*, e2023GL104759. [\[CrossRef\]](#)
21. Wang, B.; Huang, B.C.; Yang, Z.Y.; Zhang, G.W.; Liu, X.M.; Duan, L.; Armstrong, R.; Meng, Q.R. Paleomagnetic results from Early Mesozoic strata in the Qaidam Basin and their implications for the formation of the Northern China Domain. *Geophys. J. Int.* **2024**, *3*, 1621–1635. [\[CrossRef\]](#)
22. Zhao, G.C.; Cawood, P.A. Precambrian geology of China. *Precambrian Res.* **2012**, *222–223*, 13–54. [\[CrossRef\]](#)
23. Wang, T.; Zhou, Y.N.; Chai, R.Y.; Cheng, X.; Wang, P.F.; Xing, L.Y.; Li, T.; Deng, X.H.; Wu, H.N. Microcontinental block amalgamation in the northern Tibetan Plateau and its significance for understanding the closure of the Proto-Tethyan Ocean. *Palaeogeogr. Palaeoclimatol. Palaeoecol.* **2023**, *627*, 111722. [\[CrossRef\]](#)
24. Wu, D.Q.; Sun, F.Y.; Pan, Z.C.; Tian, N. Geochronology, geochemistry, and Hf isotopic compositions of Triassic igneous rocks in the easternmost segment of the East Kunlun orogenic belt, NW China; implications for magmatism and tectonic evolution. *Int. Geol. Rev.* **2021**, *63*, 1011–1029. [\[CrossRef\]](#)

25. Qinghai Bureau of Geology and Mineral Resources (QBGMR). *Regional Geological Investigation of the Dulan Area*; Bingjing: Regional Geology of Qinghai Province Supply Paper; Qinghai Bureau of Geology and Mineral Resources (QBGMR): Beijing, China, 1978; pp. 1–104. (In Chinese)
26. Kruiver, P.P.; Dekkers, M.J.; Heslop, D. Quantification of magnetic coercivity components by the analysis of acquisition curves of isothermal remanent magnetization. *Earth Planet. Sci. Lett.* **2001**, *189*, 269–276. [[CrossRef](#)]
27. Girdler, R.W. The measurement and computation of anisotropy of magnetic susceptibility of rocks. *Geophys. J. Int.* **1961**, *5*, 34–44. [[CrossRef](#)]
28. Jelinek, V. Characterization of the magnetic fabric of rocks. *Tectonophysics* **1981**, *79*, T63–T67. [[CrossRef](#)]
29. Tarling, D.H.; Hrouda, F. *The Magnetic Anisotropy of Rocks*; Chapman & Hall: London, UK, 1993; pp. 1–189.
30. Stacey, F.D.; Joplin, G.; Lindsay, J. Magnetic anisotropy and fabric of some foliated rocks from S.E. Australia. *Geofis. Pura Appl.* **1960**, *47*, 30–40. [[CrossRef](#)]
31. Balsley, J.R.; Buddington, A.F. Magnetic susceptibility anisotropy and fabric of some Adirondack granites and orthogneisses. *Am. J. Sci.* **1960**, *258*, 6–20.
32. Zijdeveld, J.D.A. AC demagnetization of rocks: Analysis of results. *Dev. Solid Earth Geophys.* **2013**, *3*, 254–286.
33. Dekkers, M.J. Magnetic properties of natural pyrrhotite. II. High- and low-temperature behavior of  $J_{rs}$  and TRM as function of grain size. *Phys. Earth Planet.* **1989**, *57*, 266–283. [[CrossRef](#)]
34. Ao, H.; Deng, C.L. Review in the identification of magnetic minerals. *Prog. Geophys.* **2007**, *2*, 432–442. (In Chinese)
35. Thompson, R.; Oldfield, F. *Environmental Magnetism*; Allen & Unwin: London, UK, 1986.
36. Dunlop, D.J.; Özdemir, Ö.; Schmidt, P.W. Paleomagnetism and paleothermometry of the Sydney Basin 2. Origin of anomalously high unblocking temperatures. *J. Geophys. Res. Solid Earth* **1997**, *102*, 27285–27295. [[CrossRef](#)]
37. Roberts, A.P.; Florindo, F.; Larrasoaña, J.C.; O’Regan, M.A.; Zhao, X. Complex polarity pattern at the former Plio–Pleistocene global stratotype section at Vrica (Italy): Remagnetization by magnetic iron sulphides. *Earth Planet. Sci. Lett.* **2010**, *292*, 98–111. [[CrossRef](#)]
38. Flinn, D. On the Symmetry Principle and the Deformation Ellipsoid. *Geol. Mag.* **1965**, *102*, 36–45. [[CrossRef](#)]
39. Hrouda, F. Magnetic anisotropy of the rocks and its application in geology and geophysics. *Geophys. Surv.* **1982**, *1*, 37–82. [[CrossRef](#)]
40. Ellwood, B.B. Analysis of emplacement mode in basalt from Deep-Sea Drilling Project holes 319A and 321 using anisotropy of magnetic susceptibility. *J. Geophys. Res.* **1975**, *80*, 4805–4808. [[CrossRef](#)]
41. Sun, J.P.; Han, F.; Deng, C.L.; Pan, Y.X. Rock magnetism and magnetic fabrics of upper Cretaceous volcanic rocks from CCSD-LK-I, in Jiaolai Basin, Shandong province. *Prog. Geophys.* **2016**, *31*, 2397–2407. (In Chinese)
42. Huang, B.C.; Piper, J.D.A.; Sun, L.S.; Zhao, Q. New paleomagnetic results for Ordovician and Silurian rocks of the Tarim Block, Northwest China, and their paleogeographic implications. *Tectonophysics* **2019**, *755*, 91–108. [[CrossRef](#)]
43. Hrouda, F.; Chadima, M. Examples of tectonic overprints of magnetic fabrics in rocks of the Bohemian Massif and Western Carpathians. *Int. J. Earth Sci.* **2020**, *109*, 1321–1336. [[CrossRef](#)]
44. Pan, X.Q.; Shen, Z.Y.; Shi, L.Q.; Zhang, Z.L. Anisotropy of magnetic susceptibility of igneous rocks. *Prog. Geophys.* **2014**, *29*, 1023–1032. (In Chinese)
45. Pan, Y.X.; Zhu, R.X. The present progress in Magnetic Fabrics. *Prog. Geophys.* **1998**, *13*, 52–59. (In Chinese)
46. Paterson, S.R.; Fowler, T.K.; Schmidt, K.L.; Yoshinobu, A.S.; Yuan, E.S.; Miller, R.B.; Clemens, J.D.; Hutton, D.H. Interpreting magmatic fabric patterns in plutons. *Lithos* **1998**, *44*, 53–82. [[CrossRef](#)]
47. Cakh-Tapia, E.; Walker, G.P.L.; Herrero-Bervera, E. The internal structure of lava flows—insights from AMS measurements I: Near-vent a’a. *J. Volcanol. Geotherm. Res.* **1996**, *1–2*, 21–36. [[CrossRef](#)]
48. Khan, M.A. The anisotropy of magnetic susceptibility of some igneous and metamorphic rocks. *J. Geophys. Res.* **1962**, *67*, 2873–2885. [[CrossRef](#)]
49. Halvorsen, E. The magnetic fabric of some dolerite intrusions, northeast Spitsbergen; implications for their mode of emplacement. *Earth Planet. Sci. Lett.* **1974**, *2*, 127–133. [[CrossRef](#)]
50. Symons, D.T.A. Age and flow direction from magnetic measurements on the historic Aiyansh flow, British Columbia. *J. Geophys. Res.* **1975**, *80*, 2622–2626. [[CrossRef](#)]
51. Vitouš, P.; Tomek, F.; Petronis, M.S. Magnetic fabrics of rhyolite ignimbrites reveal complex emplacement dynamics of pyroclastic density currents, an example from the Altenberg–Teplice Caldera, Bohemian Massif. *Bull. Volcanol.* **2022**, *84*, 75. [[CrossRef](#)]
52. Das, A.; Mallik, J.; Banerjee, S. Characterization of the magma flow direction in the Nandurbar–Dhule Deccan dyke swarm inferred from magnetic fabric analysis. *Phys. Earth Planet.* **2021**, *319*, 106782. [[CrossRef](#)]
53. Venkateshwarlu, M.; Ramesh Babu, N.; Satyakumar, A.V. Rock magnetism and anisotropy of magnetic susceptibility studies on charnockites, southern India. *Acta Geophys.* **2023**, *71*, 613–624. [[CrossRef](#)]

**Disclaimer/Publisher’s Note:** The statements, opinions and data contained in all publications are solely those of the individual author(s) and contributor(s) and not of MDPI and/or the editor(s). MDPI and/or the editor(s) disclaim responsibility for any injury to people or property resulting from any ideas, methods, instructions or products referred to in the content.